

RESEARCH ON SPINNING FORMING TECHNOLOGY OF D406A ULTRA-HIGH STRENGTH STEEL

Wu, L. M.*; Kang, Q.**,#; Zhao, H. C.*; Zhang, H.*** & Tang, M.*

* School of Intelligent Manufacturing, Geely University of China, Chengdu 641423, China

** Chengdu Runbo Technology Co., Ltd., Chengdu 610100, China

*** College of Architecture and Environment, Sichuan University, Chengdu 610065, China

E-Mail: kangquan163@163.com (# Corresponding author)

Abstract

To address issues such as significant wall thickness deviation, diameter expansion, and cracking during the spinning of D406A ultra-high strength steel cylindrical parts due to improper process parameter combinations, a finite element model for power spinning was established using ABAQUS/Explicit software. The orthogonal experiment range analysis method was employed to investigate the influence of process parameters, including spinning roller feed per revolution (1–3 mm/r), thinning ratio (30–50 %), and spinning roller nose radius (4–8 mm), on wall thickness deviation. The results indicate that the order of influence of each parameter on wall thickness deviation is as follows: thinning ratio > spinning roller feed per revolution > spinning roller nose radius. Based on simulation results, spinning experiments using the optimal parameter combination: spinning roller feed per revolution of 2 mm/r, thinning ratio of 40 %, and spinning roller nose radius of 4 mm, successfully produced a cylindrical part with a wall thickness deviation of 0.053 mm, further verifying the accuracy of the finite element simulation analysis.

(Received in October 2025, accepted in December 2025. This paper was with the authors 1 month for 1 revision.)

Key Words: D406A Ultra-High Strength Steel, Spinning Forming, Process Parameters, Wall Thickness Deviation, Thinning Ratio

1. INTRODUCTION

D406A ultra-high strength steel, derived from the material 30Si2MnCrMoVE, possesses a strength 4 to 6 times that of ordinary carbon steel. It also offers advantages such as high strength and toughness, excellent weldability, and corrosion resistance. Suitable for extreme load environments, it is widely used in aerospace rocket engine casings, aircraft structural components, high-reliability mechanical parts, and more [1].

Cylindrical parts are widely used in aerospace, national defence, military industry, and other fields, serving as important components such as missile casings, aircraft auxiliary fuel tanks, gun barrels, and mixer drums [2]. Power spinning technology, as a continuous local plastic forming process, is an effective method for producing thin-walled, high-precision cylindrical parts [3, 4]. Power spinning is a volume-forming process characterized by a significant reduction in wall thickness during deformation while the volume of the blank remains essentially unchanged. The final shape is determined by the dimensions of the mandrel, and the dimensional accuracy and geometric tolerances of the finished product depend on the rational design of process parameters. Therefore, reasonably designing spinning process parameters is key to ensuring product quality after spinning [5, 6].

Numerous scholars, both domestic and international, have conducted extensive research on the spinning forming of workpieces. Zhang et al. [7] established an elastic-plastic finite element model for thin-walled cylindrical parts made of Hastelloy C276 superalloy, studying the influence of process parameters such as the thinning ratio and mandrel rotation speed on the inner diameter deviation and wall thickness deviation during backward spinning. Zhou et al. [8] based on the finite element software ABAQUS, analysed the influence of the number of spinning rollers on the rib filling in 2219-O aluminium alloy cylindrical shells with ribs.

Lyu et al. [9] through a combination of simulation and experimentation, investigated the spinning deformation characteristics of thin-walled cylindrical parts with spiral internal ribs, analysing the stress and strain characteristics in different areas under spinning forces. Huang et al. [10] taking 304 stainless steel tubes as the research object, simulated the spinning forming process of 304 stainless steel cylindrical parts based on the Simufact Forming finite element software, obtaining the optimal forming parameter combination. Zhu et al. [11] established a spinning process model for TB6 titanium alloy cylindrical parts, using finite element software to simulate the deformation process of the workpiece under different process parameters, and comprehensively selected the optimal spinning process parameter combination. Han et al. [12] established a spinning model for TA15 titanium alloy by comprehensively considering various thermal effects, studying the deformation mechanisms of the alloy under different mechanical and thermal loads. Marghmaleki et al. [13] conducted a numerical study on the spinning process, employing a three-dimensional explicit finite element analysis method to simulate the spinning process of an aluminium circular plate and investigating the influence of thermal effects on the conventional spinning process. Roy et al. [14] performed simulations of the spinning process for aluminium alloy spherical parts based on different spinning roller trajectories, deriving a superior spinning process trajectory for spherical parts. Nakasato et al. [15] through experiments on 6063 aluminium alloy tubes, determined the influence rules of the number of passes and temperature on the wall thickness and inner wall flatness of spun parts. Gondo and Arai [16] studied the influence of path parameters and control methods on the wall thickness distribution in multi-pass conventional spinning forming of cylindrical cups. By optimizing path parameters and process conditions, precise control of thickness distribution can be achieved, avoiding early fracture problems caused by excessive thinning. Russo et al. [17] conducted the influence of part asymmetry on the achievable forming height in multi-pass spinning, methods to design the multi-pass toolpaths and the blanks required to spin both axisymmetric and asymmetric components without a mandrel are developed. Hoseini et al. [18] studied investigation of microstructure and mechanical properties of copper shell produced by shear spinning in different rotation directions, in this study, the effect of alteration in the direction of forming during the shear spinning of C11000 copper metal on mechanical properties, microstructure, texture, and anisotropy was investigated.

It can be seen from the above research that scholars have explored the influence patterns of process parameters based on numerical simulation studies of power spinning, which further guides the actual spinning forming process. However, there is currently limited research on the impact of key process parameters on the spinning forming of D406A ultra-high strength steel cylindrical parts. Therefore, this paper simulates the spinning forming process of D406A ultra-high strength steel cylindrical parts based on the finite element simulation software ABAQUS/Explicit. It investigates the influence of key process parameters such as spinning roller feed per revolution, thinning ratio, and spinning roller nose radius on the spinning forming process. The study analyses the variations in equivalent stress, equivalent strain, and workpiece wall thickness deviation during the spinning process of D406A ultra-high strength steel cylindrical parts. Through comprehensive optimization, the best combination of spinning forming process parameters is selected, thereby providing a theoretical basis for shortening the development cycle and improving the success rate of spinning.

2. FINITE ELEMENT MODEL

2.1 Geometric model establishment

The spinning forming process of the cylindrical part is simulated using forward spinning. The model consists of three components: the spinning roller, the workpiece, and the mandrel. To

reduce computation time, the model is simplified: the workpiece is defined as a three-dimensional deformable solid, while the spinning roller and the mandrel are defined as three-dimensional analytical rigid bodies. A double-cone spinning roller is used. Based on the geometric dimensions listed in Table I, the geometric models of the spinning roller, workpiece, and mandrel are created and assembled to establish the three-dimensional numerical simulation model for the cylindrical spinning forming process, as shown in Fig. 1. In this model, three spinning rollers are evenly distributed around the circumference of the workpiece, while the bottom of the workpiece is fixed to the mandrel and rotates with it around its own axis.

The specific motion principle of the process model is as follows: the mandrel serves as the primary drive, rotating at a set speed of 120 r/min, which drives the workpiece to rotate around its axis. The inner and outer sides of the workpiece come into contact with the mandrel and the spinning rollers, respectively, generating friction, with a friction coefficient of 0.2. The three spinning rollers rotate around their respective axes and, after reaching the predetermined radial position of the tube blank (determined by the thinning ratio), feed from bottom to top along the axial direction of the workpiece. Under the pressure exerted by the spinning rollers, the metal of the workpiece undergoes plastic strain flow, thereby achieving forward spinning processing.

Table I: Model geometric dimensions.

Parameters	Values
Mandrel height (mm)	150
Mandrel outer diameter (mm)	$\Phi 177$
Workpiece inner diameter (mm)	$\Phi 177$
Workpiece outer diameter (mm)	$\Phi 188.2$
Workpiece height (mm)	80
Spinning roller diameter (mm)	200
Spinning roller height (mm)	30
Spinning roller attack angle ($^{\circ}$)	22
Spinning roller relief angle ($^{\circ}$)	30

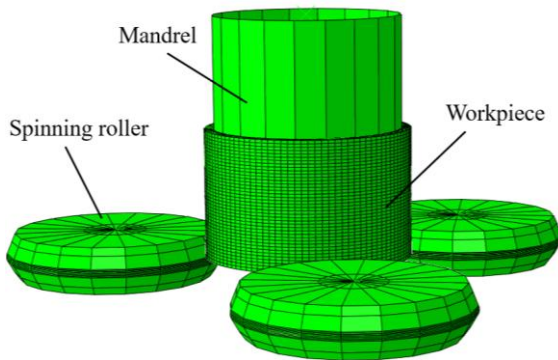


Figure 1: Three-dimensional model for numerical simulation.

2.2 Material model and mesh division

In order to accurately simulate the power spinning process of the studied cylindrical part, the true stress-true strain curve of D406A ultra-high strength steel was obtained through uniaxial tensile experiments, as shown in Fig. 2. The yield strength is 1420 MPa, and the tensile strength is 1830 MPa. The obtained true stress-true strain curve of D406A ultra-high strength steel was imported into ABAQUS, and other material parameters were set, including a density of $7850 \text{ kg}\cdot\text{m}^{-3}$, a Poisson's ratio of 0.3, and an elastic modulus of 210 GPa.

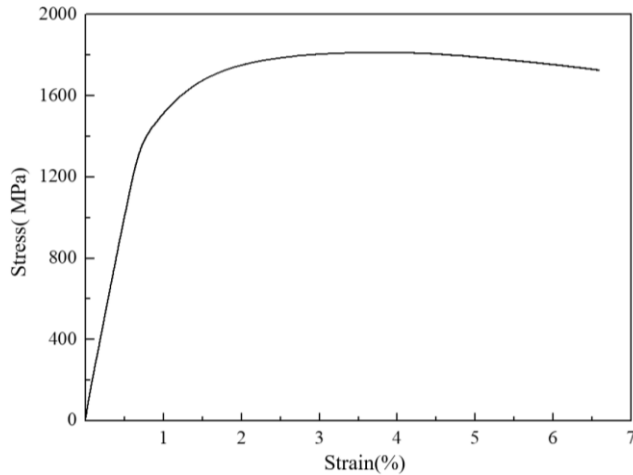


Figure 2: The true stress-true strain curve of D406A ultra-high strength steel.

The analysis step type is selected as Dynamic, Explicit. To improve computational efficiency, mass scaling technology is employed to reduce calculation time [19]. The quality of the mesh significantly affects both the computational efficiency and accuracy of the results. Hexahedral meshes are less prone to distortion during large deformations and offer high analysis accuracy. Therefore, the workpiece is meshed using the 8-node linear hexahedron, reduced integration element (C3D8R), with a total of 64,000 elements generated. The Arbitrary Lagrangian-Eulerian (ALE) adaptive meshing technique is applied, which automatically adjusts the algorithm to enhance calculation accuracy. This ensures smooth mesh changes during the deformation process, promotes more uniform material flow, and prevents excessive mesh distortion in the workpiece that could lead to solver interruption.

2.3 Model reliability verification

In ABAQUS finite element modelling, to ensure the reliability of the model, verification is typically conducted from an energy perspective by examining the ratio of kinetic energy to internal energy of the workpiece. It is required that the ratio of kinetic energy to internal energy of the blank does not exceed 0.05 for most of the forming process. The ratio of kinetic energy to internal energy for the workpiece in this model is shown in Fig. 3. At the initial stage of spinning, the curve shows slight fluctuations, which are caused by vibrations generated from friction when the workpiece first contacts the spinning rollers. After the contact stabilizes, the vibrations decrease, and the curve gradually stabilizes. Once stabilized, the ratio of the curve is significantly less than 0.01, indicating that the established spinning model is reliable.

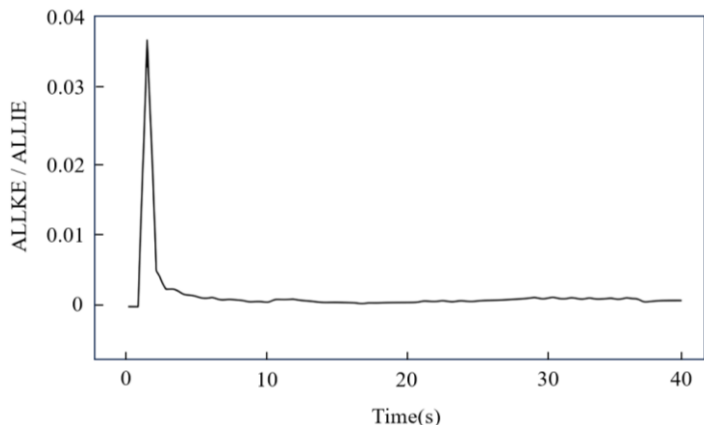


Figure 3: The ratio of kinetic energy to internal energy for the workpiece.

3. SIMULATION RESULT ANALYSIS

The spinning roller feed per revolution, thinning ratio, and spinning roller nose radius were typically set within the ranges of 1-3 mm/r, 30%–50%, and 4-8 mm, respectively. To investigate the influence of these three process parameters on the spinning process, a three-factor, three-level orthogonal experimental design (Table II) was adopted. The factors were: spinning roller feed per revolution (*A*), thinning ratio (*B*), and spinning roller nose radius (*C*). The corresponding levels were: *A* = 1.0, 2.0, 3.0 mm/r; *B* = 30 %, 40 %, 50 %; *C* = 4, 6, 8 mm. Based on this orthogonal design (Table III), nine simulation experiments were conducted using finite element simulation of the spinning process for D406A ultra-high strength steel cylindrical parts. After simulation, the influence of the process parameters on the stress/strain distribution and wall thickness deviation of the workpiece was analysed.

Table II: Orthogonal experimental factor level table.

Factor levels	Feed per revolution (<i>A</i>) (mm/r)	Thinning ratio (<i>B</i>) (%)	Spinning roller nose radius (<i>C</i>) (mm)
Level 1	1.0	30	4
Level 2	2.0	40	6
Level 3	3.0	50	8

Table III: Orthogonal experimental design scheme and simulation results.

Experiment number	Process parameter			Simulation result
	<i>A</i> (mm/r)	<i>B</i> (%)	<i>C</i> (mm)	Wall thickness deviation (mm)
T-01	1.0	30	4	0.035
T-02	1.0	40	6	0.120
T-03	1.0	50	8	0.134
T-04	2.0	30	8	0.031
T-05	2.0	40	4	0.055
T-06	2.0	50	6	0.074
T-07	3.0	30	6	0.053
T-08	3.0	40	8	0.066
T-09	3.0	50	4	0.082

3.1 Influence of simulation process parameters on stress and strain

The equivalent stress and equivalent strain distributions of the spun D406A ultra-high strength steel cylindrical parts under different simulated process parameters are shown in Figs. 4 and 5, respectively. Comparison of the nine equivalent stress contour plots (Fig. 4) indicates that the maximum equivalent stress reaches 1496 MPa, while the minimum is 1220 MPa. The overall equivalent stress in schemes T-05 and T-08 is relatively low, making them the preferred parameter combinations. Furthermore, the nine equivalent stress contour plots reveal that stress is related to the combination of various parameters and results from their coupling effects. Different parameter combinations yield distinct stress distributions. This further demonstrates that optimizing process parameter combinations through finite element simulation can achieve a favourable equivalent stress distribution, thereby preventing cracking caused by excessively high stress during the spinning process [20, 21].

Comparison of the equivalent plastic strain contours (Fig. 5) shows maximum and minimum values of 5.916 and 2.565. The maximum equivalent plastic strain consistently occurs on the workpiece surface in contact with the spinning roller. This maximum strain increases with both the spinning roller feed per revolution and the thinning ratio, confirming that these two parameters are key factors governing plastic deformation during spinning.

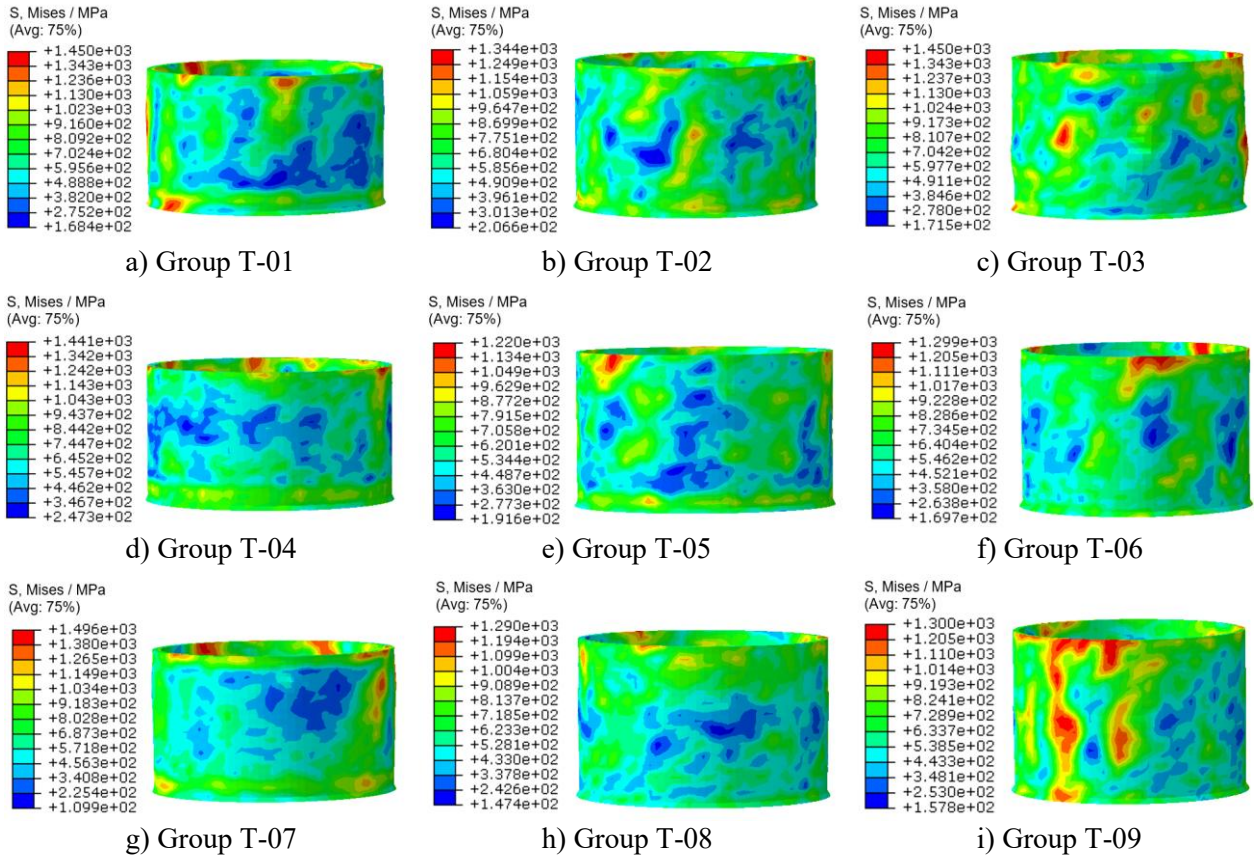


Figure 4: Equivalent stress nephograms under different simulation process parameters.

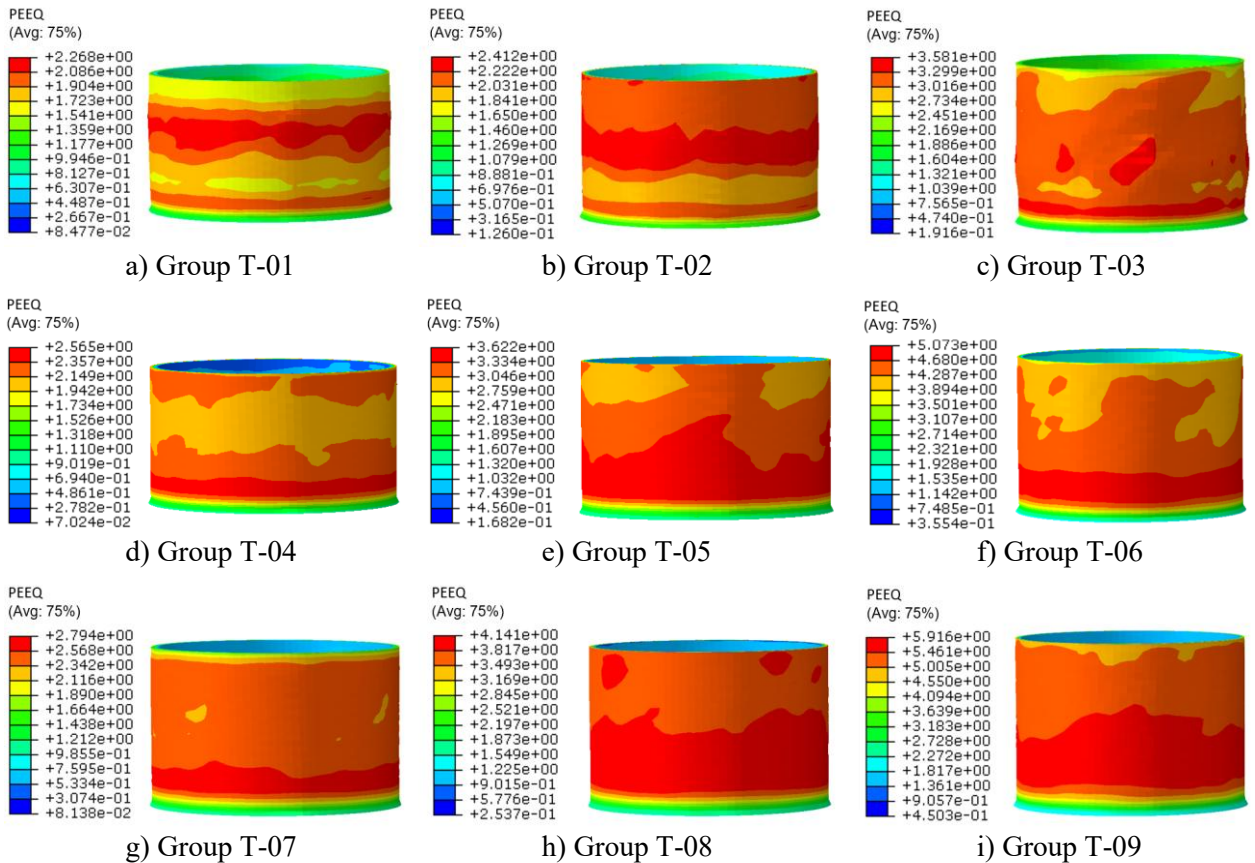


Figure 5: Equivalent plastic strain nephograms under different simulation process parameters.

3.2 The influence of simulation process parameters on wall thickness deviation

Based on the wall thickness deviation results from the simulations in Table III, the deviations for groups T-02 and T-03 have exceeded the specified range (<0.1 mm). Particularly, group T-03 shows the largest wall thickness deviation. As can be seen in the corresponding images (c) in Figs. 5 and 6, severe diameter expansion occurred, leading to significant unevenness in wall thickness. This severe expansion is caused by the mismatch between the relatively small feed per revolution (1 mm/r) and the large thinning ratio (50%). The wall thickness deviations of the remaining seven groups all meet the requirement, being less than 0.1 mm, but the specific values vary noticeably.

To further investigate the influence of each factor level on wall thickness deviation, an accurate evaluation was conducted using the range analysis method based on the orthogonal experiment simulation results from Table III, with the wall thickness deviation of the D406A ultra-high strength steel cylindrical part as the evaluation indicator. This analysis was applied to the spinning forming simulation, and the specific simulation analysis results are presented in Table IV. In the range analysis table, K_1 , K_2 , and K_3 represent the sum of the objective function values for each factor at levels 1, 2, and 3, respectively. \bar{K}_1 , \bar{K}_2 , and \bar{K}_3 are the corresponding averages of K_1 , K_2 , and K_3 . R is the range, which is the difference between the maximum and minimum values among \bar{K}_1 , \bar{K}_2 , and \bar{K}_3 . In the orthogonal experiment of the spinning numerical simulation for D406A ultra-high strength steel cylindrical parts, the significance of the influence of each relevant process parameter on the objective function is closely related to the range R . The larger the R value, the more pronounced the influence of the process parameter on the evaluation indicator [22]. Based on the range analysis results in Table IV, it is found that the order of significance of the influence of these main process parameters on the wall thickness deviation of the spun D406A ultra-high strength steel cylindrical workpiece is as follows: thinning ratio (B) $>$ spinning roller feed per revolution (A) $>$ spinning roller nose radius (C).

Table IV: Analysis results of extreme thickness difference (mm).

Range parameter	A	B	C
K_1	0.289	0.119	0.175
K_2	0.160	0.241	0.233
K_3	0.201	0.290	0.242
\bar{K}_1	0.096	0.040	0.058
\bar{K}_2	0.053	0.080	0.078
\bar{K}_3	0.067	0.097	0.081
R	0.043	0.057	0.022

According to the data in Table IV, the influence trends of these three simulation process parameters on the wall thickness deviation of the D406A ultra-high strength steel cylindrical part can be clearly observed. To better illustrate the impact of these variables on the wall thickness deviation of the D406A ultra-high strength steel cylindrical part, trend charts were used to describe the variations, as shown in Fig. 6. From Fig. 6, it can be concluded that: when the spinning roller feed per revolution is between 1-2 mm/r, the wall thickness deviation decreases as the feed per revolution increases, reaching its minimum at 2 mm/r. However, when the feed per revolution exceeds 2 mm/r, the wall thickness deviation increases with further increases in the feed per revolution. Additionally, the wall thickness deviation shows a positive correlation with both the thinning ratio and the spinning roller nose radius, meaning that the wall thickness deviation increases as the thinning ratio and spinning roller nose radius increase.

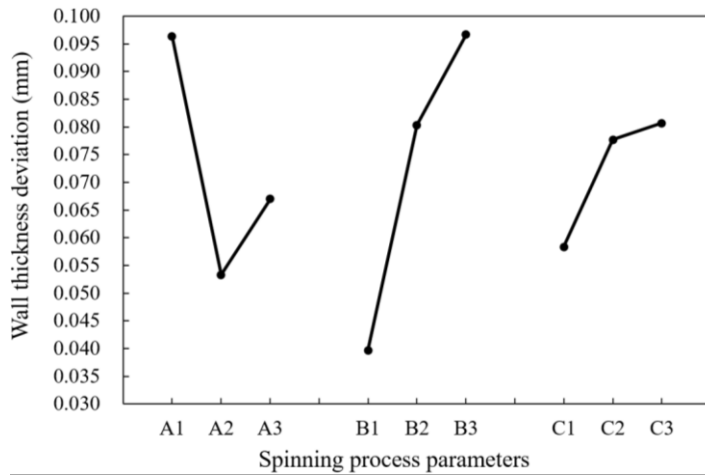


Figure 6: Graph showing the changing trend of the influence of process parameters on the wall thickness difference.

From Fig. 6, it can be concluded that the optimal combination of process parameters to achieve the optimization goal of wall thickness deviation is A2B1C1, i.e., a spinning roller feed per revolution of 2.0 mm/r, a thinning ratio of 30 %, and a spinning roller nose radius of 4 mm. However, actual production must also consider efficiency, and a higher thinning ratio contributes to improved production efficiency. Therefore, based on the results of the equivalent stress and equivalent strain simulation analyses presented earlier, the experimental data from Group T-05 in Table III are optimal. The parameters for this group are: spinning roller feed per revolution of 2.0 mm/r, thinning ratio of 40 %, and spinning roller nose radius of 4 mm. This set of parameters not only includes the optimal feed per revolution and spinning roller nose radius but also a thinning ratio of 40 %, which can effectively enhance production efficiency. Furthermore, the wall thickness deviation is 0.055 mm, meeting practical requirements, and the maximum equivalent stress is 1220 MPa, the lowest among all nine experimental groups. Consequently, the subsequent spinning experiments will adopt the optimal combination of A2B2C1. In actual manufacturing, slight adjustments may be made to these parameters to meet specific forming needs.

4. SPINNING EXPERIMENT AND RESULTS

4.1 Experimental program determination

To verify the correctness of the virtual simulation method, a spinning experiment was conducted on a D406A ultra-high strength steel cylindrical part. The inner diameter of the workpiece is $\Phi 177$ mm, and the required wall thickness after spinning is 1.4 ± 0.05 mm. Therefore, based on the above simulation analysis results, the spinning experiment plan was formulated. A three-pass spinning process was adopted. According to the total thinning ratio of 75 %, the designed blank wall thickness is 5.6 mm. Considering the springback issue of the workpiece during spinning, the thinning ratios for each pass were designed as 40 %, 40 %, and 37 %, respectively. The specific spinning process parameters of the experiment plan are detailed in Table V. For the first and second passes, a larger feed per revolution was selected as much as possible to ensure good contact between the workpiece and the mandrel, which is beneficial for controlling roundness and straightness tolerances. For the third pass, the feed per revolution was appropriately reduced to allow moderate diameter expansion of the workpiece, facilitating demoulding and avoiding scratches on the inner surface of the workpiece. After determining the machine equipment, tooling, and pre-spinning blank, the pre-spinning preparation state was completed, as shown in Fig. 7. The spinning experiment

was carried out according to the plan, and the results of the three-pass spinning process are shown in Figs. 8 a, 8 b, and 8 c, respectively.

Table V: Spinning process parameters.

Spinning pass	Feed per revolution (mm/r)	Pass thinning ratio (%)	Spinning roller nose radius (mm)
First pass	2	40	4
Second pass	2	40	4
Third pass	1.8	37	4

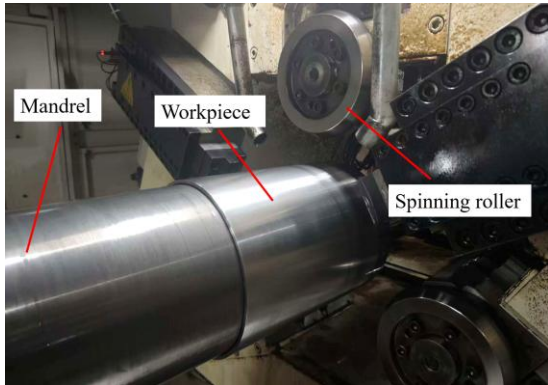


Figure 7: Preparation status diagram before spinning.

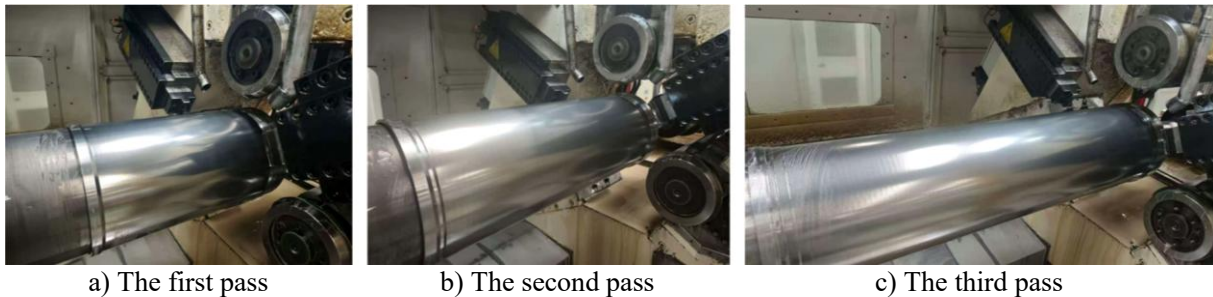


Figure 8: Result diagrams of three passes of spinning press forming.

4.2 Experimental results

The workpiece maintained good contact with the mandrel throughout the entire spinning process, with no occurrence of surface peeling or cracking. Geometric tolerances such as roundness and straightness met the design requirements, while the diameter and wall thickness dimensions exhibited strong overall convergence. The product demonstrated good overall quality, aligning well with the design specifications. The finished product after spinning is shown in Fig. 9.



Figure 9: The workpiece after the spinning process is completed.

The spun workpiece was inspected by dividing its effective axial length evenly into 8 sections (labelled A to K). Each section was further divided into 4 circumferential measurement points (labelled ① to ④) on the cross-section, as shown in Fig. 10. The wall thickness t was measured at positions ① to ④ for each section, and the results are presented in Table VI. The final wall thickness for each section was taken as the average value, denoted as t_A . The wall thickness deviation (Δt) of the entire cylindrical part was calculated as the difference between the maximum and minimum values of t_A . The measured result was 0.053 mm, which is less than the specified limit of 0.1 mm, thereby meeting the design requirements satisfactorily.

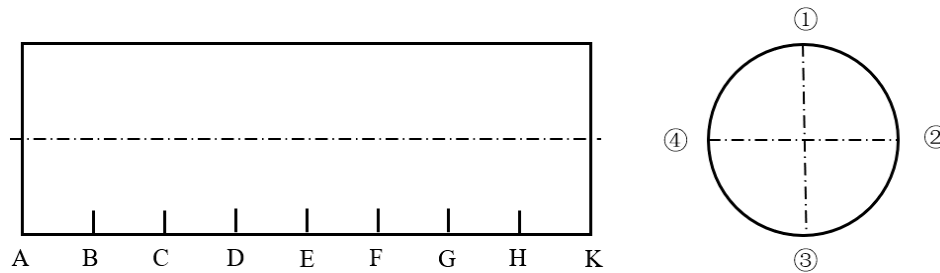


Figure 10: Measurement status diagram.

Table VI: Workpiece measurement result.

Projects	Wall thickness t (mm)				Average wall thickness t_A (mm)	Wall thickness deviation Δt (mm)
	①	②	③	④		Max (t_A) – Min (t_A)
A	1.417	1.427	1.408	1.413	1.416	0.053
B	1.424	1.446	1.417	1.410	1.424	
C	1.422	1.439	1.391	1.439	1.423	
D	1.361	1.418	1.397	1.416	1.398	
E	1.389	1.409	1.440	1.412	1.413	
F	1.424	1.446	1.437	1.399	1.426	
G	1.362	1.389	1.371	1.369	1.373	
H	1.411	1.418	1.428	1.429	1.421	
K	1.429	1.399	1.420	1.412	1.415	

5. CONCLUSION

Combined with the finite element simulation results, appropriate process parameters from the simulation were selected to conduct the power spinning experiment for the D406A ultra-high strength steel cylindrical part. The experimental results demonstrate the correctness of the finite element simulation model and the reliability of the simulation results for reference. Through the finite element simulation analysis, the following conclusions can be drawn:

(1) The equivalent stress in the power spinning of D406A ultra-high strength steel cylindrical parts is influenced by the coupled effects of multiple process parameters. Optimizing the parameter combination through finite element simulation can yield a more favourable equivalent stress distribution. The spinning roller feed per revolution and the thinning ratio are the key parameters governing plastic deformation during spinning, with the equivalent plastic strain increasing as these two parameters rise.

(2) The influence of each process parameter on the wall thickness deviation of the spun D406A ultra-high strength steel cylindrical part is ranked in the following order of significance: thinning ratio > spinning roller feed per revolution > spinning roller nose radius.

(3) As the spinning roller feed per revolution increases from 1 mm/r to 3 mm/r, the wall thickness deviation of the spun part first decreases and then increases, reaching a minimum at

2 mm/r. Furthermore, the wall thickness deviation increases with an increase in both the thinning ratio and the spinning roller nose radius.

(4) By integrating finite element analysis with practical considerations and based on the simulation results of equivalent stress, equivalent strain, and wall thickness deviation for various parameters – while also accounting for actual production efficiency – the optimal parameter combination was selected: a spinning roller feed per revolution of 2.0 mm/r, a thinning ratio of 40 %, and a spinning roller nose radius of 4 mm.

(5) Finite element simulation proves to be an effective and feasible method for determining the optimal parameter combination in the power spinning of D406A ultra-high strength steel. It helps ensure processing quality and shortens the development cycle.

ACKNOWLEDGEMENT

The research described in this paper was financially supported by the Geely University of China high-level research project cultivation program.

REFERENCES

- [1] Su, C.-W.; Wang, A.-G.; Feng, H.-Q.; Xu, X.-C.; Liu, Y.-L. (2022). Development status of forming process based on aviation metal parts, *Aerospace Materials & Technology*, Vol. 52, No. 5, 21-34, doi:[10.12044/j.issn.1007-2330.2022.05.004](https://doi.org/10.12044/j.issn.1007-2330.2022.05.004)
- [2] Miao, P.-Z.; Zhu, X.-B.; Hu, C.-L.; Sun, H.-Q.; Xiao, X.-Q.; Zhao, Z. (2014). Finite element modeling and optimization analysis on power spinning of the thin-wall cylinder, *Forging & Stamping Technology*, Vol. 39, No. 9, 137-142, doi:[10.13330/j.issn.1000-3940.2014.09.027](https://doi.org/10.13330/j.issn.1000-3940.2014.09.027)
- [3] Bylya, O. I.; Khismatullin, T.; Blackwell, P.; Vasin, R. A. (2018). The effect of elasto-plastic properties of materials on their formability by flow forming, *Journal of Materials Processing Technology*, Vol. 252, 34-44, doi:[10.1016/j.jmatprotec.2017.09.007](https://doi.org/10.1016/j.jmatprotec.2017.09.007)
- [4] Sugita, Y.; Arai, H. (2015). Formability in synchronous multipass spinning using simple pass set, *Journal of Materials Processing Technology*, Vol. 217, 336-344, doi:[10.1016/j.jmatprotec.2014.11.017](https://doi.org/10.1016/j.jmatprotec.2014.11.017)
- [5] Guo, Y.-M.; Xu, H.-Q.; Xue, X.-Q.; Wang, D.; Zheng, Y.; Wang, Y.; Huang, T.; Zhao, X.; Liang, C.-L. (2021). Power spinning process of thin-walled shell parts for 2A12 aluminum alloy, *Forging & Stamping Technology*, Vol. 46, No. 5, 143-150, doi:[10.13330/j.issn.1000-3940.2021.05.022](https://doi.org/10.13330/j.issn.1000-3940.2021.05.022)
- [6] Chen, S. W.; Zhan, M.; Gao, P. F.; Ma, F.; Zhang, H. R. (2021). A new robust theoretical prediction model for flange wrinkling in conventional spinning, *Journal of Materials Processing Technology*, Vol. 288, Paper 116849, 12 pages, doi:[10.1016/j.jmatprotec.2020.116849](https://doi.org/10.1016/j.jmatprotec.2020.116849)
- [7] Zhang, T.; Li, X.-H.; Wei, Z.; Chang, S.-W. (2017). Influence of process parameters on the flow forming quality of thin-walled tube with large diameter-thickness ratio, *Journal of Plasticity Engineering*, Vol. 24, No. 2, 75-81
- [8] Zhou, Y.; Zhao, Y.; Yu, Z.-Q.; Zhao, Y.-X. (2022). Numerical simulation of stagger spinning of cylindrical part with cross inner ribs, *Journal of Shanghai Jiaotong University*, Vol. 56, No. 1, 62-69, doi:[10.16183/j.cnki.jsjtu.2020.326](https://doi.org/10.16183/j.cnki.jsjtu.2020.326)
- [9] Lyu, W.; Zhan, M.; Wang, P.; Ma, F.; Gao, P.-F. (2021). Deformation mechanism in flow forming of thin-walled tube with helical grid-stiffened ribs, *Aerospace Materials & Technology*, Vol. 51, No. 4, 104-108, doi:[10.12044/j.issn.1007-2330.2021.04.011](https://doi.org/10.12044/j.issn.1007-2330.2021.04.011)
- [10] Huang, M.-Z.; Guo, Y.-M.; Zheng, Y.; Xu, H.-Q.; Huang, T.; Lu, S.-X. (2025). Simulation analysis and experimental study on spinning of 304 stainless steel cylindrical parts, *Forging & Stamping Technology*, Vol. 50, No. 2, 178-184, doi:[10.13330/j.issn.1000-3940.2025.02.022](https://doi.org/10.13330/j.issn.1000-3940.2025.02.022)
- [11] Zhu, E.-R.; Cui, X.; Guo, L.-L.; Ouyang, D.-L. (2023). Simulation on power spinning process for TB6 titanium alloy cylindrical parts, *Forging & Stamping Technology*, Vol. 48, No. 2, 126-134, doi:[10.13330/j.issn.1000-3940.2023.02.016](https://doi.org/10.13330/j.issn.1000-3940.2023.02.016)

- [12] Han, D.; Zhan, M.; Yang, H. (2013). Deformation mechanism of TA15 shells in hot shear spinning under various load conditions, *Rare Metal Materials and Engineering*, Vol. 42, No. 2, 243-248, doi:[10.1016/S1875-5372\(13\)60039-9](https://doi.org/10.1016/S1875-5372(13)60039-9)
- [13] Marghmaleki, I. S.; Beni, Y. T.; Noghrehabadi, A. R.; Kazemi, A. S.; Abadyan, M. (2011). Finite element simulation of thermomechanical spinning process, *Procedia Engineering*, Vol. 10, 3769-3774, doi:[10.1016/j.proeng.2011.04.616](https://doi.org/10.1016/j.proeng.2011.04.616)
- [14] Roy, B. K.; Korkolis, Y. P.; Arai, Y.; Araki, W.; Iijima, T.; Kouyama, J. (2021). A study of forming of thin-walled hemispheres by mandrel-free spinning of commercially pure aluminum tubes, *Journal of Manufacturing Processes*, Vol. 64, 306-322, doi:[10.1016/J.JMAPRO.2020.12.036](https://doi.org/10.1016/J.JMAPRO.2020.12.036)
- [15] Nakasato, S.; Kobayashi, J. Itoh, G. (2018). Hot spinning formability of aluminum alloy tube, *Procedia Manufacturing*, Vol. 15, 1263-1269, doi:[10.1016/j.promfg.2018.07.360](https://doi.org/10.1016/j.promfg.2018.07.360)
- [16] Gondo, S.; Arai, H. (2022). Effect and control of path parameters on thickness distribution of cylindrical cups formed via multi-pass conventional spinning, *Journal of Intelligent Manufacturing*, Vol. 33, No. 2, 617-635, doi:[10.1007/s10845-021-01886-W](https://doi.org/10.1007/s10845-021-01886-W)
- [17] Russo, I. M.; Cleaver, C. J.; Allwood, J. M.; Loukaides, E. G. (2020). The influence of part asymmetry on the achievable forming height in multi-pass spinning, *Journal of Materials Processing Technology*, Vol. 275, Paper 116350, 16 pages, doi:[10.1016/j.jmatprotec.2019.116350](https://doi.org/10.1016/j.jmatprotec.2019.116350)
- [18] Hoseini, S. M. J.; Ghayour, H.; Golazani, A. S.; Asgarani, M. K.; Ebrahimzadeh, I. (2021). Investigation of microstructure and mechanical properties of copper shell produced by shear spinning in different rotation directions, *Materials Research Express*, Vol. 8, No. 6, Paper 066521, 14 pages, doi:[10.1088/2053-1591/ac0923](https://doi.org/10.1088/2053-1591/ac0923)
- [19] Khan, M. A. A.; Sheikh, A. K. (2021). Simulation-based mould design, life prediction and reliability assessment of a valve body, *International Journal of Simulation Modelling*, Vol. 20, No. 2, 219-230, doi:[10.2507/IJSIMM20-2-543](https://doi.org/10.2507/IJSIMM20-2-543)
- [20] Yang, L.; Wang, L. Y.; Li, L.; Zheng, X. H.; Chang, S. Y. (2025). A simulation-based optimization approach to enhance drive shaft fatigue strength, *International Journal of Simulation Modelling*, Vol. 24, No. 1, 123-134, doi:[10.2507/IJSIMM24-1-CO1](https://doi.org/10.2507/IJSIMM24-1-CO1)
- [21] Šugár, P.; Šugárová, J.; Zemko, P. (2012). Strain and strain-hardening analysis of formed parts produced by multi-pass metal spinning, *Technical Gazette*, Vol. 19, No. 1, 111-114
- [22] Wu, D.; Zhao, C. L.; Huang, C. L.; Luo, X. (2025). Micro-texture optimization for titanium cutting tools via simulation, *International Journal of Simulation Modelling*, Vol. 24, No. 2, 333-344, doi:[10.2507/IJSIMM24-2-CO7](https://doi.org/10.2507/IJSIMM24-2-CO7)